

# Vessels as 4D Curves: Global Minimal 4D Paths to Extract 3D Tubular Surfaces

Hua Li     Anthony Yezzi

School of ECE, Georgia Institute of Technology, Atlanta, GA, USA

{hua.li, ayezzi}@ece.gatech.edu

## Abstract

*In this paper, we propose an innovative approach to the segmentation of tubular or vessel-like structures which combines all the benefits of minimal path techniques (global minimizers, fast computation, powerful incorporation of user input) with some of the benefits of active surface techniques (representation of a full 3D tubular surface rather than a just curve). The key is to represent the trajectory of the vessel not as a 3D curve but to go up a dimension and represent the entire vessel as a 4D curve, where each 4D point represents a 3D sphere (three coordinates for the center point and one for the radius). The 3D vessel structure is then obtained as the envelope of the family of spheres traversed along this 4D curve. Because the 3D surface is simply a curve in 4D, we are able to fully exploit minimal path techniques to obtain global minimizing trajectories between two user supplied end-points in order to reconstruct vessels from noisy or low contrast 3D data without the sensitivity to local minima inherent in most active surface techniques. In contrast to standard purely spatial 3D minimal path techniques, however, we are able to represent the full vessel surface rather than just a curve which runs through its interior. Our representation also yields a natural notion of a vessel's "central curve", which is obtained by tracing the center points of the family of 3D spheres rather than its envelope. We demonstrate the utility of this approach on 2D images of roads as well as both 2D and 3D MR angiography and CT images.*

## 1. Introduction

Medical image segmentation is an essential and important step for clinical tasks such as 3D organ visualization, diseases diagnosis, surgery planning, and so on. Numerous segmentation methods were proposed depending on the organ structures, imaging modalities, application domains, user-interaction requirements, and other specific factors [6, 18, 10, 21].

During the past twenty years, the extraction of vascular objects such as the blood vessel, coronary artery, human pulmonary tree, abdominal aorta, vascular structure in legs and livers, and colon has attracted the attention of more and more researchers. Various methods such as filtering methods [13, 28, 26, 23], model-based methods [5, 12], mathematical morphology methods [32, 33], region-growing methods [29], vessel tracking methods [30, 20], level set evolution methods [16, 3, 27, 17, 19] were proposed. More details can be found in the surveys [10, 21, 15].

Some of these previous methods extract the vessel surfaces directly, and then use thinning algorithms to generate a centerline. Other methods were proposed to extract only a centerline (or skeleton), thereby requiring further processing to obtain the 3D shape. Deschamps and Cohen [9] reduced the problem of generating a centerline to the problem of finding the minimal paths in 3D images. The minimal path technique proposed by Cohen et al. [8, 7] captures the global minimum curve of an active contour model's energy between two user supplied end-points. By defining the image as an oriented graph characterized by its cost function (or potential), the boundary segmentation problem becomes an optimal path search problem between these two points in the graph. This leads to the global minimum of the energy function and thereby avoids the local minima problem in edge-based active contour models [31, 4]. Fast Marching schemes [25] were used by the authors to improve the computational time. In [9], the authors were able to center the minimal path inside the object by adding the term of the Euclidean distance function to the boundary into the cost function.

The minimal path approach [8] has several advantages such as finding global minima, fast computation, ease of implementation, and more powerful incorporation of user input<sup>1</sup>. Such advantages are lacking in most surface evolu-

<sup>1</sup> Surface evolution approaches generally make use of user input only for obtaining seed points from which to start evolving the initial surface. This is fundamentally different from minimal path techniques which are specifically designed to fully trust and exploit the initial user input, guaranteeing its incorporation into the final answer as well.

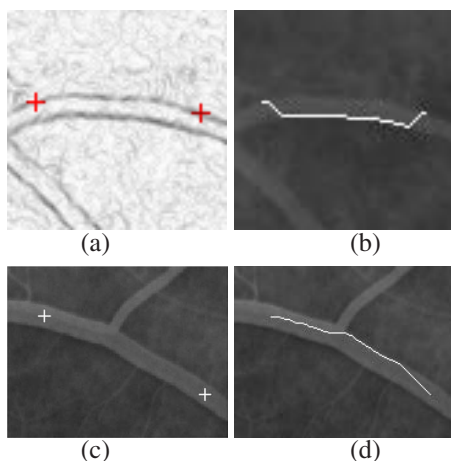


Figure 1. Two disadvantages in the classic minimal path technique. Panel (a) shows the negative gradient information ( $255 - \nabla I$ ) and the two initial points (the red crosses). Panel (b) shows the original image with the extracted boundary (the white line). Since the searching principle of the minimal path technique is just along the fastest gradient descent, the path may drop down to the wrong boundary nearby. Panel (c) shows another original image and the two initial points (the red crosses). Panel (d) shows the extracted inaccurate central path (the white line). When the potential inside the object is constant or does not vary much, the minimal path will be the shortest Euclidean path and is often tangential to the edges. The potential is  $P(p) = 10 + |\nabla I(p)|^2$  for the up row,  $P(p) = 10 + |I(p) - I(p_0)|$  for the bottom row.  $I(p)$ ,  $I(p_0)$  are the intensities of point  $p$  and the starting point  $p_0$  (the left cross).  $\nabla I$  is the image gradient information.

tion techniques (whether they be level set or finite element approaches) with the problem of local minima being particularly troublesome in most cases. Surface evolution techniques do have one nice advantage, though: When they are successful, they capture and represent the vessel surfaces directly, not just some path running through their interior as in the minimal path approach. This is particularly important in cases where one wishes to measure changes in vascular thickness at different places along the vessel.

Unfortunately, despite their numerous advantages, traditional minimal path techniques exhibit some disadvantages both in general and in the particular application of vessel segmentation. First, *vessel boundary* extraction can be exceedingly difficult, even in 2D where the longitudinal cross-sectional boundary of a vessel may be completely described by two curves (see Fig. 1). Even if the two user supplied end-points are located exactly on the same desired boundary, the minimal path may jump temporarily to a different nearby boundary and return at some later point as a sort of “short cut” to reduce the total cost of the path. This is illustrated in Fig. 1 (a)-(b).

Second, *vessel interior* extraction does not always yield a trajectory that remains central to the vessel. Since inten-

sity based potentials don’t vary greatly between different points within the vessel interior, the minimal path tends to favor trajectories of shortest Euclidean distance within the tubular structure, often yielding paths that run tangential to vessel boundaries rather than central to their interior. This undesirable property is shown here in Fig. 1 (c)-(d), and again later in Fig. 3 (d) and (h). This affects applications such as virtual endoscopy, where subsequent path centering methods [9] are required to readjust a traditionally extracted, purely spatial minimal path in order to obtain a central trajectory for virtual fly-through.

Finally, in 3D (just as in 2D), traditional purely spatial minimal path techniques can be used only for curve extraction, whereas vessels and other tubular structures, despite sharing some characteristics with curves, are surfaces. In [2], the authors proposed a 3D surface extraction method. It models the desired surface as an infinite set of 3D minimal paths that join individual points between two user supplied curves. This approach, which was not designed for vessels, would struggle in capturing long winding vessel boundaries for the reasons illustrated in Fig. 1 (a)-(b), not to mention its rather complex implementation.

We will instead propose a new variant of the the traditional, purely spatial minimal path technique by incorporating an additional *non-spatial* dimension into the search space. The resulting algorithm, in contrast to [2], will require us to search for a *single*, global minimal path between user supplied endpoints in this higher dimension. The detected path will capture directly and simultaneously the *central curve* of the extracted vessel as well as the 3D *vessel surface*. As such, we will keep all of the benefits of purely spatial minimal path techniques as well as one of the primary benefits of active contour and surface evolution techniques.

The key is to model a vessel, or any other tubular surface, as a 4D curve rather than a purely spatial 3D curve. Each point on the 4D curve will consist of three spatial coordinates plus a fourth coordinate which describes the thickness (radius) of the vessel at that corresponding 3D point in space. Thus, each 4D point represents a sphere in 3D space, and the vessel is obtained by taking the envelope of these spheres as we move along the 4D curve. We may instead take the center points of this family of spheres if we wish to reconstruct the central path rather than the surface of the detected tubular structure. Like traditional spatial minimal path algorithms, we may exploit techniques such as Fast Marching to keep the computational time down. The implementation is a straight-forward 4D version of the the 3D implementation, and is therefore extremely simple. We will demonstrate the utility of this approach on 2D images of roads as well as both 2D and 3D MR angiography and CT images.

## 2. Tubular Surface Extraction

### 2.1. BackgroundGlobal Minimal Paths

In this subsection, we present the basic idea of the minimal path technique introduced by Cohen, Kimmel and coauthors [8, 7]. Their method is a boundary extraction approach which detects the global minimum of an active contour model's energy between two user supplied end-points, and avoids the local minima problem arising from the sensitivity to the initializations in geodesic active contours [31, 4]. The energy functional in the snake model [14] combines the smoothing terms and the image feature attraction term (potential  $P$ ),

$$E(C) = \alpha \int_0^1 \|C'(s)\|^2 ds + \beta \int_0^1 \|C''(s)\|^2 ds + \lambda \int_0^1 P(C(s)) ds, \quad (1)$$

where the parameters  $\alpha$ ,  $\beta$ , and  $\lambda$  are real positive weighting constants, the curve  $C(s) \in \mathbb{R}^n$  is a parameterized curve, and the potential  $P(C)$  is an image feature attraction term. In the minimal path technique, contrary to Eq. 1 in the snake model [14], a simplified energy minimization model,

$$E(C) = \int_{\Omega} \{\omega + P(C(s))\} ds = \int_{\Omega} \tilde{P}(C) ds, \quad (2)$$

was proposed without the second derivative term, where  $s$  represents the arc-length parameter on a defined domain  $\Omega = [0, 1]$ ,  $C(s) \in \mathbb{R}^n$  represents a curve, and  $\|C'(s)\| = 1$ ,  $E(C)$  represents the energy along the curve  $C$ ,  $P$  is the potential associated to the image,  $\omega$  is a real positive constant, and  $\tilde{P} = P + \omega$ . Energy  $E(C)$  includes the internal regularization energy (the smoothing terms) in the potential  $P$ , and controls the smoothness of the result using the potential and the constant  $\omega > 0$ .

Given a potential  $P > 0$  that takes lower values near the desired boundary, the objective of the minimal path technique is to look for a path along which the integral of  $\tilde{P} = P + \omega$  is minimal. This integral is the global minimum of  $E(C)$  between two user supplied end-points.

In [8], a minimal action map  $U_0(p)$  is defined as the minimal energy integrated along a path between the starting point  $p_0$  and any point  $p$ ,

$$U_0(p) = \inf_{A_{p_0,p}} \left\{ \int_{\Omega} \tilde{P}(C(s)) ds \right\} = \inf_{A_{p_0,p}} \{E(C)\}, \quad (3)$$

where  $A_{p_0,p}$  is defined as the set of all paths between the point  $p_0$  and  $p$ . The value of each point  $p$  in this minimal action map  $U_0(p)$  corresponds to the minimal energy integrated along a path starting from the point  $p_0$  to the point  $p$ . So, the minimal path between the point  $p_0$  and the point  $p$  can be easily deduced by calculating this action map  $U_0(p)$

and then sliding back from the point  $p$  to the point  $p_0$  on the action map  $U_0$  according to the gradient descent.

In order to compute the minimal action map  $U_0(p)$ , they also formulated a PDE equation,

$$\frac{\partial L(v, t)}{\partial t} = \frac{1}{P} \vec{n}(v, t), \quad (4)$$

to describe the set of equal energy contours  $L$  in “time”  $t$ , where  $t$  represents the height of the level sets  $L$  of  $U_0$ , and  $\vec{n}(v, t)$  is the normal to the closed curve  $L(v, t)$ . These curves  $L(v, t)$  correspond to the set of points  $p$ , and the values of  $U_0(p)$  on these points are equal to  $t$ . Eq. 4 evolves a front starting from an infinitesimal circle around  $p_0$  until each point inside the image domain is assigned a value for  $U_0$  [8]. The family of curves  $L(v, t)$  constructs the level sets of the surface  $U_0(p)$ . Because the action map  $U_0$  has only one minimum value at the starting point  $p_0$  and increases from the starting point outwards, it can be determined by solving the Eikonal equation

$$\|\nabla U_0\| = \tilde{P} \quad \text{with} \quad U_0(p_0) = 0. \quad (5)$$

In [8], they described three methods to compute this map  $U_0$ , which are all consistent with the continuous propagation rule while implemented on a rectangular grid. These three methods are the level set front propagation approach [1], the shape from shading approach [22, 11], and the fast marching approach [24]. They used the fast marching method to calculate  $U_0$  because of its lower complexity than that of the other two methods.

### 2.2. Generalization: Tubular Surface Extraction

As already discussed in Section 1, the traditional *spatial* minimal path technique does not apply for the detection of surfaces or regions. However, for the special case of vessels and other tubular surfaces, we may generalize these approaches by representing a *3D vessel surface* as a *4D curve* and using a corresponding minimal path algorithm in 4D. As such, we keep all of the benefits of minimal path techniques (global minima, fast implementations, full incorporation of user input) while adding the ability to represent and detect the vessel surface directly, which so far has been a feature restricted to active contour and surface techniques.

We will represent the surface of the vessel or tubular structure as the envelope of a one-parameter family (curve) of spheres with different centers (three coordinates) and different radii (fourth coordinate). This representation is illustrated in Fig. 2. In this way, the *3D surface* extraction problem is translated into the problem of finding a *4D curve* which encodes this family of 3D spheres.

We now modify Eq. 2 to a new energy minimization

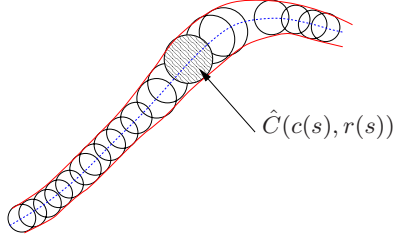


Figure 2. We present a tubular surface as the envelope of a family of spheres with continuously changing center points and radii.

model which relates to 3D spheres rather than 3D points,

$$\begin{aligned} E(\hat{C}) &= \int_{\Omega} \{\omega + P(\hat{C}(c(s), r(s)))\} ds \\ &= \int_{\Omega} \tilde{P}(\hat{C}) ds, \end{aligned} \quad (6)$$

where  $s$  still represents the arc-length parameter over an interval  $\Omega$ ,  $c(s)$  represents the location of a point in the original image domain  $\Omega_I$  either in  $\mathbb{R}^2$  [ $c(s) = (x(s), y(s))$ ] or in  $\mathbb{R}^3$  [ $c(s) = (x(s), y(s), z(s))$ ],  $r(s) \in [0, r_{max}]$  represents the radius of the circle/sphere centered at  $c(s)$  ( $r_{max}$  is the largest allowed thickness of the vessel to be captured),  $\hat{C}(c(s), r(s)) \in \Omega_I$  represents a “path” composed by a family of circles/spheres in  $\Omega_I$ , in which  $c(s)$  are the center points and  $r(s)$  are the radii of the spheres,  $E(\hat{C})$  represents the energy which is the integral of  $\tilde{P}$  along  $\hat{C}(c(s), r(s))$ ,  $P$  is the potential related to the image properties,  $\omega$  is a real positive constant, and  $\tilde{P} = P + \omega$ . In this manner,  $E(\hat{C})$  also includes the internal regularization energy (smoothing terms) in the potential  $P$ , and the smoothness of the result can be controlled by the potential and the constant  $\omega > 0$ .

Traditionally, the potential  $P$  is a *pointwise* image measurement. Here, instead, we design  $P$  as a measurement which incorporates the full set of image values within the sphere surrounding the corresponding image point. We define any sphere in the image domain  $\Omega_I$  as  $sp = (p, r)$ , where  $p$  is the center point and  $r$  is the radius. In designing the potential  $P$  related to such spheres in the image, we should keep in mind that the entire sphere should lie inside the desired object and be as big as possible (so that it is tangential to the object boundary). Such spheres should exhibit lower values of  $P$  compared to smaller spheres which lie inside the desired object or any sphere which lies outside (fully or partially) the desired object.

Given a potential  $P$  that satisfies the above conditions (we will give two example potentials later) and two user supplied spheres  $sp_0$  and  $sp_1$  which mark the beginning and ending locations (and radii) of the vessel or tubular object, our goal is to find a family of spheres  $\hat{C}$  such that  $\hat{C}(c(0), r(0)) = sp_0$  and  $\hat{C}(c(1), r(1)) = sp_1$  and such that the integral along  $\hat{C}$  of  $\tilde{P} = P + \omega$  is minimal. The

vessel interior then modeled by the union of the interiors of all the spheres along  $\hat{C}$ , its surface is modeled by the envelope of the spheres along  $\hat{C}$ , and its centerline by the centers of the spheres along  $\hat{C}$ . In addition, the varying thickness of the vessel may be read directly using the radii of the spheres along  $\hat{C}$ .

The principle of this surface extraction method is similar to that of the spatial minimal path technique [8]. There are two problems to solve. The first is how to minimize this energy functional shown in Eq. 6. In particular, can we still define the minimal action map and use fast marching methods to calculate it? The second one is how to formulate an appropriate potential  $P$  satisfying the discussed design conditions.

A sphere  $sp = (p, r)$  in image domain  $\Omega_I$  corresponds to a point  $\hat{p}$  in a new domain  $\Omega_{I,r} = \Omega_I \times [0, r_{max}]$ . Here, the sphere’s radius  $r \in \mathbb{R}^1$  is added as the additional fourth coordinate in  $\Omega_{I,r}$ . In this way, each point on the 4D curve consists of three spatial coordinates plus a fourth coordinate which represents the radius of the 3D sphere. The initial 3D sphere  $sp_0$  is the 4D point  $\hat{p}_0$ , and the final 3D sphere  $sp_1$  is the 4D point  $\hat{p}_1$ . The problem of finding a family of spheres  $\hat{C}$  in 3D is translated to the problem of finding an optimal curve in 4D with  $\hat{p}_0$  and  $\hat{p}_1$  as its end points (optimal meaning that along this 4D path the integral of  $\tilde{P} = P + \omega$  is minimal).

At any 4D point  $\hat{p}$ , we may define the minimal action map  $U_0(\hat{p})$  as the minimal energy integrated along any possible path between the starting point  $\hat{p}_0$  and the point  $\hat{p}$ ,

$$\begin{aligned} U_0(\hat{p}) &= \inf_{A_{\hat{p}_0, \hat{p}}} \left\{ \int_{\Omega} \tilde{P}(\hat{C}(c(s), r(s))) ds \right\} \\ &= \inf_{A_{\hat{p}_0, \hat{p}}} \{E(\hat{C})\}, \end{aligned} \quad (7)$$

( $A_{\hat{p}_0, \hat{p}}$  is defined as the set of all paths between  $\hat{p}_0$  and  $\hat{p}$ ). The minimal path between the point  $\hat{p}_0$  and the point  $\hat{p}$  can be deduced from this action map  $U_0(\hat{p})$  shown in Eq. 7 by calculating  $U_0(\hat{p})$  and then sliding back from the point  $\hat{p}$  on the action map  $U_0$  to the point  $\hat{p}_0$  according to gradient descent. Finally, the 3D surface of the tubular structure is obtained as the envelope of the family of spheres traversed along this 4D minimal path.

So, we are able to fully exploit the minimal path technique to obtain minimizing trajectories between two end-points. Similar to that shown in subsection 2.1, we formulate a PDE equation to describe the set of equal energy contours  $L$  in “time”  $t$ . These contours  $L(v, t)$  correspond to the set of points  $\hat{p}$  for which the minimal action map  $U_0(\hat{p})$  is  $t$ . The action map  $U_0(\hat{p})$  can be determined by solving the Eikonal equation,

$$||\nabla U_0|| = \tilde{P} \quad \text{with} \quad U_0(\hat{p}_0) = 0, \quad (8)$$

using the fast marching algorithm introduced by Sethian et al. [25]. Since the 2D (or 3D) sphere is a point in 3D (or



4D), we should use a 3D (or 4D) fast marching scheme to solve the Eikonal equation and calculate the action map for 2D (or 3D) spheres.

### 2.3. Analysis of The Proposed Method

In Section 2.2, we described our tubular surface extraction method. It was very simple once the observation that a 3D tubular surface can be modeled as a 4D curve was made. As such, we may use very standard numerical algorithms to calculate a minimal path in one higher dimension to obtain a direct representation of the tubular surface itself. In this section, we offer some choices for the 4D potential  $P$ , as well as address the front propagation scheme, the algorithm complexity, and its relationship with classical spatial minimal path techniques.

The appropriate potential  $P$  is the most important factor for obtaining accurate surface extraction results. The potential  $P$  is an image feature attraction item and should be decided according to the properties of the spheres in the image. We expect that  $P$  yields the smallest values for largest possible spheres which are fully inside the desired object. For tubular objects in medical imaging such as vessels and colons, the intensity inside the object is often fairly constant (at least within small sections of the “tube”) We may exploit this property to design two sample potentials and test them in Section 3.

For an image  $I$ , and any image point  $p$  with gray value  $I(p)$ , we define the mean value  $\mu(sp)$  and the variance  $\sigma^2(sp)$  of the sphere  $sp = (p, r)$  as

$$\begin{aligned}\mu(sp) &= \frac{\int_{B(p,r)} I(\tilde{p}) d\tilde{p}}{\int_{B(p,r)} d\tilde{p}}, \\ \sigma^2(sp) &= \frac{\int_{B(p,r)} (I(\tilde{p}) - \mu(sp))^2 d\tilde{p}}{\int_{B(p,r)} d\tilde{p}},\end{aligned}\quad (9)$$

where  $B(p, r)$  represents the whole sphere. We then propose a sample potential

$$\begin{aligned}\tilde{P}(\hat{p}) = \tilde{P}(sp) &= w + \lambda_1(|\mu(sp)/r - \mu(sp_0)/r_0|^2) \\ &+ \lambda_2(|\sigma^2(sp)/r - \sigma^2(sp_0)/r_0|^2),\end{aligned}\quad (10)$$

where  $\mu(sp_0)$  and  $\sigma^2(sp_0)$  represent the mean and variance of the starting sphere  $sp_0$ ,  $w$  is the constant to control the smoothness of the path,  $\lambda_1$  and  $\lambda_2$  are two constants.

Since the gray value of the point inside the vessel is constant or does not vary much, we weight the mean and variance by  $r$  to keep the detected sphere as big as possible. When the radius is bigger than the width of the tubular structure, the mean and the variance change dramatically. This potential satisfies the conditions discussed above and is a region-based potential.

Now we give a second example potential based on boundary information. We define  $\partial B(p, r)$  to represent the

boundary of the sphere  $sp$ , use it to replace  $B(p, r)$  in Eq. 9, and calculate the mean and variance only on the boundary of the sphere  $sp$ . Then we define the mean difference  $\delta_\mu(sp)$  and the variance difference  $\delta_{\sigma^2}(sp)$  of the sphere  $sp = (p, r)$  and the sphere  $sp' = (p, r - 1)$  are

$$\begin{aligned}\delta_\mu(sp) &= |\mu(sp) - \mu(sp')|, \\ \delta_{\sigma^2}(sp) &= |\sigma^2(sp) - \sigma^2(sp')|.\end{aligned}\quad (11)$$

We propose the second sample potential

$$\tilde{P}(\hat{p}) = \tilde{P}(sp) = w + \frac{\lambda_1}{1 + \delta_\mu^2(sp)} + \frac{\lambda_2}{1 + \delta_{\sigma^2}^2(sp)}, \quad (12)$$

which also satisfies the condition discuss above, and considers the boundary information of the vessel structure.

After deciding the potential, we use the fast marching method to solve Eq. 8 and obtain the minimal action map  $U$ . The fast marching method relies on a one-sided derivative that looks in the up-wind direction of the moving front, and thereby avoids the over-shooting associated with finite differences [25]. For the 4D Eikonal equation, we need to solve

$$\begin{aligned}\left[ \begin{aligned} &(u - \min\{U_{x-1,y,z,r}, U_{x+1,y,z,r}, 0\})^2 + \\ &(u - \min\{U_{x,y-1,z,r}, U_{x,y+1,z,r}, 0\})^2 + \\ &(u - \min\{U_{x,y,z-1,r}, U_{x,y,z+1,r}, 0\})^2 + \\ &(u - \min\{U_{x,y,z,r-1}, U_{x,y,z,r+1}, 0\})^2 \end{aligned} \right] \\ = \tilde{P}^2(x, y, z, r)\end{aligned}\quad (13)$$

according to the 4D Fast Marching Evolution Scheme. In this fast marching scheme, the algorithm's complexity is  $O(N \log N)$  and  $N$  is the number of 4D grid points. Further details and the proof of the complexity is shown in [25]. We may keep  $N$  small by limiting the range of the radius coordinate and discretizing it to just a few different values.

So the minimal “path” between the point  $\hat{p}_0$  and the point  $\hat{p}_1$  can be deduced by sliding back from the point  $\hat{p}_1$  to the point  $\hat{p}_0$  on the action map  $U_0(\hat{p})$  according to the gradient descent. It is the global minimum of the energy model shown in Eq. 6 between the two initial points.

Since we represent the entire vessel as a 4D curve, where each 4D point represents a 3D sphere. The 3D vessel structure is then obtained as the envelope of the family of spheres traversed along this 4D curve from noisy or low contrast 3D data without the sensitivity to local minima inherent in most active surface techniques.

According to the potential discussed above, all the spheres on the detected minimal “path” are tangential to the object boundary, so the union of the center points  $c(s)$  should be located on the central path of the tubular structure. We may easily obtain the centered path by tracing the center points of the family of 3D spheres rather than its envelope.

The classical minimal path technique can be treated as a special issue of our proposed method by setting the radius

of the sphere to a constant 0. However, as demonstrated in the upcoming experiments, it is much better to perform the minimal path procedure fully in 4D in order to obtain the actual vessel surfaces as well as their central paths. Supporting examples are shown in next Section 3.

### 3. Experimental Results and Analysis

The method explained previously is very useful when used for tubular structure extraction. In this section, we demonstrate our approach on various 2D and 3D simulated and real images. For each test, the user needs to specify the center positions and radii of the starting and ending points, the potential, and the largest allowed radius of the tubular object.

#### 3.1. Experiments on 2D Images

In Fig. 3, we first present the segmentation results on one 2D binary images with two different pairs of initial spheres. The image size is  $350 \times 200$ . The radii of the left and right spheres  $r_{left} = 10$  and  $r_{right} = 7$  respectively, and  $r_{max} = 15$  are for the image in panel (a).  $r_{left} = 10$ ,  $r_{right} = 9$ ,  $r_{max} = 15$  are for the image in panel (e). For these two segmentations, we use the potential defined by Eq. 10 with  $\omega = 1$ ,  $\lambda_1 = 10$ , and  $\lambda_2 = 10$ . For comparison, we also show in panel (d) and (h) the path extraction results (the red lines) by the standard 2D minimal path technique with potential  $P = 10 + |\nabla I|^2$ , where  $I$  is the image intensity,  $\nabla I$  is the image gradient information.

In Fig. 4, we present the segmentation results on one 2D noisy projection of an angiogram with two different pairs initializations (obviously, one should segment the 3D data, but here we can illustrate the accuracy of the result since the full 2D curve may be superimposed on the 2D projection image data). The image sizes are  $350 \times 200$ . In panel (a),  $r_{left} = 10$ ,  $r_{right} = 2$ , and  $r_{max} = 15$ . In panel (e),  $r_{left} = 5$ ,  $r_{right} = 5$ , and  $r_{max} = 15$ . For these two segmentations, we used the potential defined by Eq. 10 with  $\omega = 10$ ,  $\lambda_1 = 0$ , and  $\lambda_2 = 70$  for panel (a), with  $\omega = 1$ ,  $\lambda_1 = 30$ , and  $\lambda_2 = 70$  for panel (e). For comparison, we also show in panel (d) and (h) the path extraction results (the white lines) by the standard purely spatial 2D minimal path technique with potential  $P = 10 + |\nabla I|^2$ , where  $I$  means image intensity,  $\nabla I$  is the image gradient information.

In Fig. 5, we present the segmentation result on one 2D real road image, in which the road edge is blur. The image size is  $710 \times 750$ ,  $r_{left} = 3$ ,  $r_{right} = 5$ ,  $r_{max} = 8$  are set for the initializations in panel (a), here we select  $r_{left}$  and  $r_{right}$  a little smaller for calculating more accurate region information. For this segmentation, we use the potentials defined by Eq. 10 with  $\omega = 20$ ,  $\lambda_1 = 10$ , and  $\lambda_2 = 10$ .

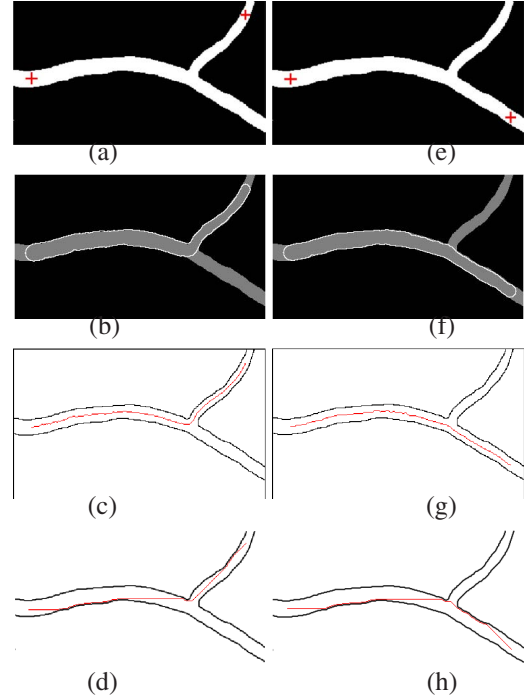


Figure 3. The surface extraction results on a 2D synthetic image. Panel (a) and (e) show the binary images with initializations. The centers of the initial spheres are shown with the red crosses. The white lines in panel (b) and (f) show the surface extraction results from our method. The red lines in panel (c) and (g) show the extracted central paths from our method. The red lines in panel (d) and (h) show the path extraction results from the standard 2D minimal path technique.

#### 3.2. Experiments on 3D Images

In this subsection, we demonstrate our method on a 3D CT dataset of the coronary artery. In Fig. 6, the original image size is  $180 \times 260 \times 200$  after is cropped. For this test, we set five pairs initialization.  $r_0 = 4$ ,  $r_1 = 1$ ,  $r_{max} = 7$  is set for segmenting the left anterior descending artery (also obtaining part of the left main coronary artery) and the left obtuse marginal artery,  $r_0 = 3$ ,  $r_1 = 1$ ,  $r_{max} = 7$  are set for segmenting the left circumflex artery with a subbranch,  $r_0 = 1$ ,  $r_1 = 1$ ,  $r_{max} = 5$  is set for segmenting the subbranch of the left obtuse marginal artery. The potential is defined by Eq. 12 with  $\omega = 10$ ,  $\lambda_1 = 10$ , and  $\lambda_2 = 10$ . Although the presented results here are the primary ones, we still can see that this method extract the desired surfaces successfully.

### 4. Conclusions and Future Work

In this paper, we present a novel 3D tubular surface extraction method that not only keeps all the benefits of standard minimal path techniques, but combines some of the benefits of active surface techniques by representing the full

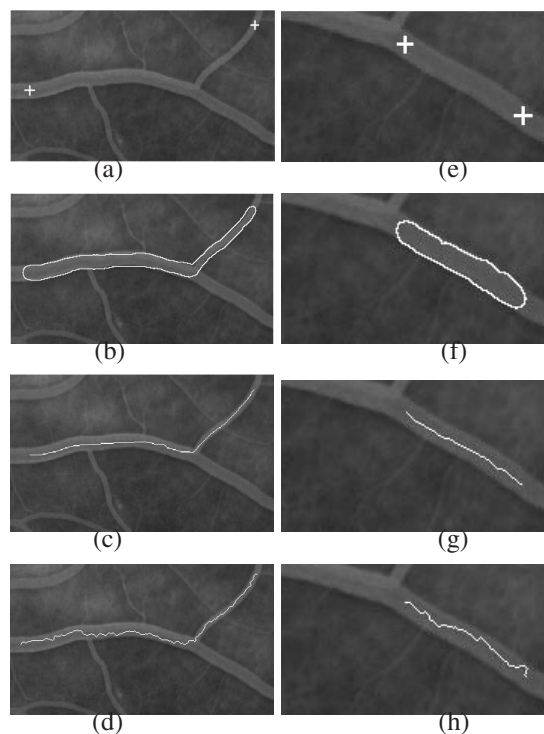


Figure 4. The surface extraction results on a real angiogram image. Panel (a) and (e) show the binary images with initializations. The centers of the initial spheres are shown with the red crosses. The white lines in panel (b) and (f) show the surface extraction results from our method. The white lines in panel (c) and (g) show the extracted central paths from our method. The white lines in panel (d) and (h) show the path extraction results from the standard 2D minimal path technique.



Figure 5. The road extraction result on a real map image. Panel (a) show the real image with initialization. The centers of the initial spheres are shown with red crosses. Panel (b) shows the road extraction result (the red lines).

3D tubular surface rather than a just curve within its interior. We are able to fully exploit minimal path techniques to obtain global minimizing trajectories between two user supplied end-points in order to reconstruct vessels from noisy or low contrast 3D data, and also yield the central path of the tubular structure simultaneously.

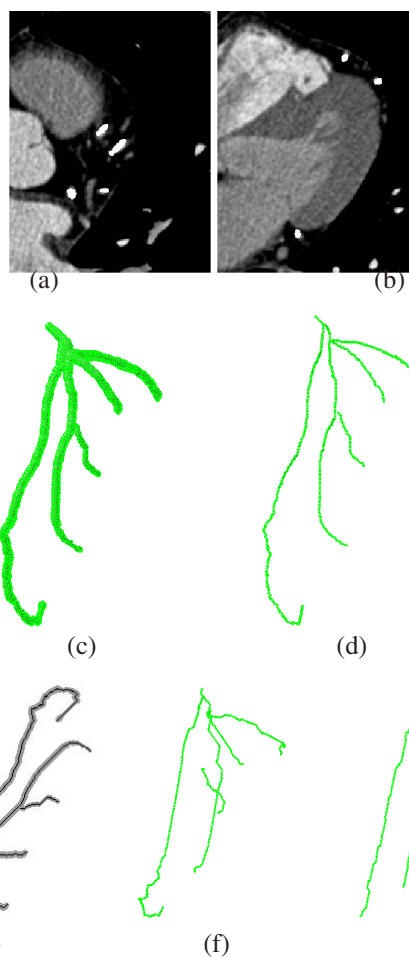


Figure 6. The segmentation results of the left main coronary artery on one 3D CT image. Panel (a) and (b) show the segmentation results on two 2D slices from our method. Panel (c) shows the reconstructed 3D model of the segmented left main coronary artery, the left anterior descending artery, the left obtuse marginal artery with one subbranch from our method. Panel (d) shows the 3D model of the corresponding central path from our method. Panel (e) shows the projection of the segmented 3D surface and the central path from our method. For comparison, panel (f) and (g) show the minimal path results from the standard 3D minimal path technique [8]. We use the center points of the initial spheres used for the tests in panel (d) as the initializations for the tests in panel (f) and (g). Because the standard 3D minimal path technique only yields a 3D curve, the extracted trajectories results are less accurate (due to the short-cutting phenomenon discussed in the introduction). The potential is  $P(p) = 10 + |\nabla I(p)|^2$  for panel (f). The potential is  $P(p) = 10 + |\nabla I(p) - \nabla I(p_0)|$  for panel (g).  $|\nabla I(p)|$  is the image gradient information.

In the future, we hope to find more appropriate choices of potentials for objects with non-uniform gray-level contrast. We will also work on the general volumetric region extraction techniques to more tubular structures, such as the

tubular structure with branches. We will also work on the medical validation of our proposed method.

## References

- [1] D. Adalsteinsson and J. Sethian. A fast level set method for propagating interfaces. *Journal of Computational Physics*, 118(2):269–277, 1995. 3
- [2] R. Ardon and L. Cohen. Fast constrained surface extraction by minimal paths. In *International Conference on Computer Vision-Workshop on VLISM*, pages 233–244, 2003. 2
- [3] S. Bouix, K. Siddiqi, and A. Tannenbaum. Flux driven automatic centerline extraction. *Medical Image Analysis*, 9(3):209–221, 2005. 1
- [4] V. Caselles, R. Kimmel, and G. Sapiro. Geodesic active contours. *International Journal of Computer Vision*, 22(1):61–79, 1997. 1, 3
- [5] A. Chung, A. Noble, and P. Summers. Vascular segmentation of phase contrast magnetic resonance angiograms based on statistical mixture modeling and local phase coherence. *IEEE Transactions on Medical Imaging*, 23(12):1490–1507, 2004. 1
- [6] L. Clarke et al. MRI segmentation: Methods and applications. *Magnetic Resonance Imaging*, 13(3):343–368, 1995. 1
- [7] L. Cohen. Multiple contour finding and perceptual grouping using minimal paths. *Journal of Mathematical Imaging and Vision*, 14(3):225–236, 2001. 1, 3
- [8] L. Cohen and R. Kimmel. Global minimum for active contour models: A minimal path approach. *International Journal of Computer Vision*, 24(1):57–78, 1997. 1, 3, 4, 7
- [9] T. Deschamps and L. Cohen. Fast extraction of minimal paths in 3D images and applications to virtual endoscopy. *Medical Image Analysis*, 5(4):281–299, 2001. 1, 2
- [10] J. Duncan and N. Ayache. Medical image analysis: Progress over two decades and the challenges ahead. *IEEE Transactions on Pattern Analysis and Machine Intelligence*, 22(1):85–105, 2000. 1
- [11] P. Dupuis and J. Oliensis. An optimal control formulation and related numerical methods for a problem in shape reconstruction. *Annals of Applied Probability*, 4(2):287–346, 1994. 3
- [12] A. Frangi, W. Niessen, R. Hoogeveen, T. van Walsum, and M. Viergever. Model-based quantitation of 3D magnetic resonance angiographic images. *IEEE Transactions on Medical Imaging*, 18(10):946–956, 1999. 1
- [13] G. Gerig, O. Kbler, R. Kikinis, and F. Jolesz. Nonlinear anisotropic filtering of MRI data. *IEEE Transactions on Medical Imaging*, 11(2):221–232, 1992. 1
- [14] M. Kass, A. Witkin, and D. Terzopoulos. Snakes: Active contour models. *International Journal of Computer Vision*, 1(4):321–332, 1988. 3
- [15] C. Kirbas and F. Quek. A review of vessel extraction techniques and algorithms. *ACM Computing Surveys (CSUR)*, 36(2):81–121, 2004. 1
- [16] L. Lorigo, O. Faugeras, W. Grimson, R. Keriven, R. Kikinis, A. Nabavi, and C. Weston. CURVES: Curve evolution for vessel segmentation. *Medical Image Analysis*, 5(3):195–206, 2001. 1
- [17] R. Manniesing et al. Level set based cerebral vasculature segmentation and diameter quantification in CT angiography. *Medical Image Analysis*, 10(2):200–214, 2006. 1
- [18] T. McInerney and D. Terzopoulos. Deformable models in medical image analysis: A survey. *Medical Imaging Analysis*, 1(2):91–108, 1996. 1
- [19] D. Nain, A. Yezzi, and G. Turk. Vessel segmentation using a shape driven flow. In *MICCAI04*, volume LNCS 3216, pages 51–59, 2004. 1
- [20] S. Olabarriaga, M. Breeuwer, and W. Niessen. Minimum cost path algorithm for coronary artery central axis tracking in CT images. In *MICCAI*, volume 2879, pages 687–694, 2003. 1
- [21] D. Pham, C. Xu, and J. Prince. Current methods in medical image segmentation. *Annual Review of Biomedical Engineering, Annual Reviews*, 2:315–337, 2000. 1
- [22] E. Rouy and A. Tourin. A viscosity solutions approach to shape-from-shading. *SIAM Journal of Numerical Analysis*, 29(3):867–884, 1992. 3
- [23] Y. Sato, J. Chen, et al. Automatic extraction and measurement of leukocyte motion in microvessels using spatiotemporal image analysis. *IEEE Transactions on Biomedical Engineering*, 44(4):225–236, 1997. 1
- [24] J. Sethian. A fast marching level set method for monotonically advancing fronts. *Proceedings of the National Academy of Science of USA*, 93(4):1591–1595, 1996. 3
- [25] J. Sethian. Fast marching methods. *SIAM Review*, 41(2):199–235, 1999. 1, 4, 5
- [26] M. Sonka, G. Reddy, M. Winniford, and S. Collins. Adaptive approach to accurate analysis of small-diameter vessels in cineangiograms. *IEEE Transactions on Medical Imaging*, 16(1):87–95, 1997. 1
- [27] A. Vasilevskiy and K. Siddiqi. Flux maximizing geometric flows. *IEEE Transactions on Pattern Analysis and Machine Intelligence*, 24(12):1565–1578, 2002. 1
- [28] A. Wahle, E. Wellnhofer, I. Mugaragu, H. Saner, H. Oswald, and E. Fleck. Assessment of diffuse coronary artery disease by quantitative analysis of coronary morphology based upon 3D reconstruction from biplane angiograms. *IEEE Transactions on Medical Imaging*, 14(2):230–241, 1995. 1
- [29] S. Wan and W. Higgins. Symmetric region growing. *IEEE Trans on Image Processing*, 12(9):1007–1015, 2003. 1
- [30] O. Wink, W. Niessen, and M. Viergever. Multiscale vessel tracking. *IEEE Trans on Medical Imaging*, 23(1):130–133, 2004. 1
- [31] A. Yezzi, S. Kichenassamy, A. Kumar, P. Olver, and A. Tannenbaum. A geometric snake model for segmentation of medical imagery. *IEEE Transactions on Medical Imaging*, 16(2):199–209, 1997. 1, 3
- [32] P. Yim, P. Choyke, and R. Summers. Gray-scale skeletonization of small vessels in magnetic resonance angiography. *IEEE Transactions on Medical Imaging*, 19(6):568–576, 2000. 1
- [33] F. Zana and J. Klein. Segmentation of vessel-like patterns using mathematical morphology and curvature evaluation. *IEEE Transactions on Image Processing*, 10(7):1010–1019, 2001. 1